High-Resolution Infrared Spectroscopy in the 1200−1300 cm^{-1} Region and Accurate Theoretical Estimates for the Structure and Ring-Puckering Barrier of Perfluorocyclobutane†

Thomas A. Blake,‡ Eric D. Glendening,§ Robert L. Sams,‡ Steven W. Sharpe,‡ and Sotiris S. Xantheas*,‡

Chemical and Materials Sciences Division, Pacific Northwest National Laboratory, P.O. Box 999, MS K8-88, Richland, Washington 99352, and Department of Chemistry, Indiana State University, Terre Haute, Indiana 47809

Received: March 30, 2007

We present experimental infrared spectra and theoretical electronic structure results for the geometry, anharmonic vibrational frequencies, and accurate estimates of the magnitude and the origin of the ring-puckering barrier in C_4F_8. High-resolution (0.0015 cm^{-1}) spectra of the ν_{12} and ν_{13} parallel bands of perfluorocyclobutane (*c*-C_4F_8) were recorded for the first time by expanding a 10% *c*-C_4F_8 in helium mixture in a supersonic jet. Both bands are observed to be rotationally resolved in a jet with a rotational temperature of 15 K. The ν_{12} mode has b_2 symmetry under D_{2d} that correlates to a_{2u} symmetry under D_{4h} and consequently has $\pm \leftarrow \pm$ ring-puckering selection rules. A rigid rotor fit of the ν_{12} band yields the origin at 1292.56031(2) cm^{-1} with $B' = 0.0354137(3)$ cm^{-1} and $B'' = 0.0354363(3)$ cm^{-1}. The ν_{13} mode is of b_2 symmetry under D_{2d} that correlates to b_{2g} under D_{4h}, and in this case, the ring-puckering selection rules are $\pm \leftarrow \mp$. Rotational transitions from the ground and first excited torsional states will be separated by the torsional splitting in the ground and excited vibrational states, and indeed, we observe a splitting of each transition into strong and weak intensity components with a separation of approximately 0.0018 cm^{-1}. The strong and weak sets of transitions were fit separately again using a rigid rotor model to give ν_{13}(strong) = 1240.34858(4) cm^{-1}, $B' = 0.0354192(7)$ cm^{-1}, and $B'' = 0.0354355(7)$ cm^{-1} and ν_{13}(weak) = 1240.34674(5) cm^{-1}, $B' = 0.0354188(9)$ cm^{-1}, and $B'' = 0.0354360(7)$ cm^{-1}. High-level electronic structure calculations at the MP2 and CCSD(T) levels of theory with the family of correlation consistent basis sets of quadruple-ζ quality, developed by Dunning and co-workers, yield best estimates for the vibrationally averaged structural parameters r(C−C) = 1.568 Å, $r(C-F)_\alpha$ = 1.340 Å, $r(C-F)_\beta$ = 1.329 Å, α(F−C−F) = 110.3°, θ_z(C−C−C) = 89.1°, and δ(C−C−C−C) = 14.6° and rotational constants of $A = B = 0.03543$ cm^{-1} and $C = 0.02898$ cm^{-1}, the latter within 0.00002 cm^{-1} from the experimentally determined values. Anharmonic vibrational frequencies computed using higher energy derivatives at the MP2 level of theory are all within <27 cm^{-1} (in most cases <5 cm^{-1}) from the experimentally measured fundamentals. Our best estimate for the ring-puckering barrier at the CCSD(T)/CBS (complete basis set) limit is 132 cm^{-1}. Analysis of the C_4F_8 electron density suggests that the puckering barrier arises principally from the $\sigma_{CC} \rightarrow \sigma_{CF}$* hyperconjugative interactions that are more strongly stabilizing in the puckered than in the planar form. These interactions are, however, somewhat weaker in C_4F_8 than in C_4H_8, a fact that is consistent with the smaller barrier in the former (132 cm^{-1}) with respect to the latter (498 cm^{-1}).

I. Introduction

The manner in which the interaction between angle and torsional strain influences the molecular structure, the internal motions, and the internal vibrational redistribution (IVR) spectra of small cyclic molecules has been of intense interest to chemists for the past 50 years.[1−4] Planar ring structures typically possess considerable angle strain, which increases as the ring buckles or puckers. Repulsive forces between neighboring, nonbonded substituent atoms, however, are at a maximum when the molecule is planar and decrease as the ring puckers. The degree of planarity of the ring in these compounds is determined, in large part, on how these forces are balanced. In many cases, this arrangement is not static and the ring oscillates via a large amplitude, low-frequency mode between two equivalent puckered equilibrium structures through a planar structure. This motion is typically hindered by a quartic−quadratic potential barrier and results in a splitting of the low-frequency puckering energy levels, a fact that imposes a distinctive sideband structure to the molecule's fundamental vibrational transitions. More recently, spectroscopic studies have aimed toward understanding the coupling between high-frequency stretching modes and hindered, low-frequency ones and how these couplings affect the IVR rates.

Among many of these systems that have been studied before, cyclobutane (*c*-C_4H_8) has received considerable attention since it may be thought of as a prototype for the four member ring compounds. In particular, it has been of interest as a means of

† Part of the "Thom H. Dunning, Jr., Festschrift".

* To whom correspondence should be addressed. E-mail: sotiris.xantheas@pnl.gov.

‡ Pacific Northwest National Laboratory.

§ Indiana State University.

10.1021/jp072521f CCC: $37.00
Published on Web 07/06/2007

understanding how changing one or more substituent atoms on the ring alters the tunneling barrier through changes in torsional forces and the reduced mass of the tunneling coordinate. Several of the fully substituted analogues, such as *c*-C_4Cl_8, *c*-$C_4(OH)_8$, and *c*-C_4F_8, have been studied in the infrared (IR) region, but their small rotational constants and high density of rovibrational-puckering states have made the assignment and analysis of their spectra difficult. Clearly, elucidating the spectroscopy of *c*-C_4H_8 is a prerequisite to understanding its fully fluorinated analogues, and consequently, we briefly summarize the progress in the IR spectroscopy of cyclobutane.

A puckered equilibrium structure of D_{2d} symmetry for *c*-C_4H_8 should exhibit Raman and IR band coincidences for 12 (those with b_2 and e symmetry) out of its 23 fundamental modes. In contrast, in a planar structure of D_{4h} symmetry, no such coincidences should occur, or perhaps only a few by accident. Indeed, early spectroscopic studies of the gas-, liquid-, and solid-phase spectra did identify the required coincidences supporting a puckered equilibrium structure of D_{2d} symmetry. It was assumed that the molecule tunneled through a finite barrier between the two equivalent puckered structures of D_{2d} symmetry, via a planar configuration of D_{4h} symmetry. This inversion splitting leads to a doubling of each vibrational energy level with respect to the rigid, puckered equilibrium structure (although the equilibrium structure of cyclobutane is D_{2d}, the appropriate permutation−inversion group for the nonrigid molecule is D_{4h}, and energy levels will be labeled accordingly). Such tunneling was certainly clear from microwave and far-IR studies of cyclobutane derivatives such as 1,1-difluorobutane, cyclobutanone, or silacyclobutane, but for the nonpolar cyclobutane, these tunneling effects would have to be observed in association with the mid-IR fundamentals.

The ring-puckering mode, ν_6 (b_{2u}), of *c*-C_4H_8 at 200 cm^{-1} is IR inactive and only weakly Raman active. Although it cannot be directly observed in the IR spectrum, the puckering mode reveals itself as a series of combination or hot bands associated with the fundamental bands. This so-called sideband structure arises from transitions from either the ground-state ring-puckering levels $0^{\pm}$ or from excited ring-puckering levels $n^{\pm}$ that may be populated. Here, $\pm$ refers to the symmetry of the ring-puckering level and the selection rule is either $\pm \leftarrow \mp$ or $\pm \leftarrow \pm$, depending on the symmetry of the associated vibrational transition. A detailed examination of the IR spectrum of the ν_{14} (b_{1g}) CH_2 scissoring mode at 1453 cm^{-1} by Stone and Mills[5] showed a number of these transitions that are spread out over a range of 150 cm^{-1} to the red and 200 cm^{-1} to the blue of the fundamental's origin obeying the selection rules $\pm \leftarrow \mp$, and $\Delta n = 0$ or ± 1. The ν_{18} (e_g) CH_2 symmetric stretch mode at 2878 cm^{-1}, recorded by Ueda and Shimanouchi[6] and re-examined by Stone and Mills,[5] also showed these sideband transitions that were spread out over 100 cm^{-1} to the red of the band origin. Stone and Mills[5] furthermore pointed out that other b_{1g} and e_g symmetry vibrational modes should exhibit a similar sideband structure, but because of the weakness of the bands, either obscuring from other bands or the more diffuse nature of the perpendicular bands, they were not able to assign a ring-puckering sideband structure to any other IR active fundamental bands. The a_{2u} and e_u symmetry IR active bands have the $\pm \leftarrow \pm$ ring-puckering selection rule, and the sideband structure in these cases would very nearly be superimposed. Assuming separability of the ring-puckering coordinate from the rest of the vibrational coordinates and constant reduced mass, they were able to assign ring-puckering transitions to a one-dimensional quartic−quadratic potential with a barrier height of 503 cm^{-1} for the ground state and 491 cm^{-1} for the ν_{14}, $v = 1$ excited state.

Malloy and Lafferty[7] reassigned some of the ring-puckering transitions reported by Stone and Mills, and Miller and Capwell[8] reported those for *c*-C_4H_8 and *c*-C_4D_8 using a model that included the coordinate dependence of the reduced mass. Their conclusion was that the constant-reduced mass model was adequate for determining barrier heights with the data set then available but that the vibrational and isotopic dependence of these barrier heights neglected zero-point effects and vibrational coupling with other modes. They also pointed out that improvements in data quality that would allow for a more precise determination of the band centers and vibrational dependence of rotational constants would warrant inclusion of the coordinate-dependent reduced mass kinetic energy term, mode coupling terms, and sixth-order ring-puckering potential energy terms in the Hamiltonian.

IR and electron diffraction experiments by Kuchitsu and coworkers[9] have determined the rotational constants for several of the ring-puckering states, and more accurate bond lengths and angles including the dihedral angle between the CCC planes on opposite sides of the ring and the CH_2 tilt angle formed between the bisectors of the adjacent CCC and HCH planes. Further analysis of the data has shown a significant coupling between the methylene rocking and the ring-puckering motions. They also performed room and dry ice temperature IR spectroscopy of static cell samples of *c*-C_4H_8 using Fourier transform infrared (FTIR) and diode laser spectroscopy. For the ν_{14} band (b_{1g}), for which the ring-puckering selection rules are $\pm \leftarrow \mp$, they observed not only transitions from the $\nu_{14} + \nu_6 - \nu_6$ ($1^- \leftarrow 1^+$) and $\nu_{14} + \nu_6 - \nu_6$ ($1^+ \leftarrow 1^-$) hot bands that were red-shifted by 0.5 and 1 cm^{-1} from the ν_{14} band origin ($0^- \leftarrow 0^+$) but also a band originating from the 0^- ring-puckering state ($0^+ \leftarrow 0^-$), which is red-shifted by 0.02 cm^{-1} from the ($0^- \leftarrow 0^+$) band. Rotational transitions from the two fundamental bands were resolved, assigned, and fit separately from the Doppler limited spectrum. For the ν_{16} band (a_{2u}), the ring-puckering selection rules are $\pm \leftarrow \pm$ and any difference between the ($0^+ \leftarrow 0^+$) and ($0^- \leftarrow 0^-$) fundamental bands or the $\nu_{16} + \nu_6 - \nu_6$ ($1^+ \leftarrow 1^+$) and $\nu_{16} + \nu_6 - \nu_6$ ($1^- \leftarrow 1^-$) hot bands cannot be resolved at the Doppler limit.

As mentioned above, little detailed information regarding the higher frequency fundamentals was available from the room-temperature spectra of *c*-C_4H_8 because of considerable spectral congestion. The extreme degree of cooling afforded by supersonic jet expansions and the considerable improvement in sensitivity and resolution available with IR lasers should make this region more accessible. Indeed, Li et al.[10] recorded a jet spectrum of the ν_{12} band of *c*-C_4H_8 seeded in helium using an F-center laser. Their spectrum, centered at 2981 cm^{-1}, showed four bands, two weak and two strong, with rotational structure. They assigned these bands as originating from the 0^+ and 0^- ring-puckering states and terminating in the excited CH_2 asymmetric stretching state that is anharmonically coupled to a dark state. This coupling leads to a splitting of the excited state where each state has the 0^+ and 0^- puckering levels, thus leading to the four observed bands. Rotational analysis of each of the bands shows different *J*-dependent perturbations, a fact suggesting that there is further coupling to a manifold of dark states with different coupling selection rules.

Our previous theoretical studies[11,12] of the structure, harmonic, and anharmonic spectroscopic constants and puckering barrier of cyclobutane (*c*-C_4H_8) suggested that accurate estimates of

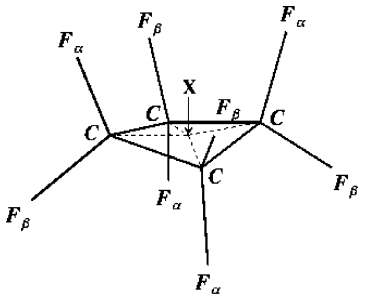

D_{2d}

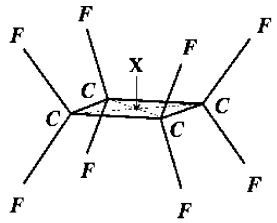

D_{4h}

Figure 1. Conformations of the minimum (D_{2d}) and transition state (D_{4h}) geometries of c-C_4F_8.

the ring-puckering barrier require a combination of higher levels of electron correlation and very large orbital basis sets. By performing CCSD(T) calculations with basis sets as large as quintuple-ζ quality, we were able to obtain, for the first time, a value for the puckering barrier within 10 cm^{-1} (or 2%) from the experimental estimate whereas the best previously calculated values were in errors exceeding 40%. Our best estimate of 498 cm^{-1} for the puckering barrier of c-C_4H_8 was in excellent agreement with the one originally suggested by Stone and Mills[5] (503 cm^{-1}). It was furthermore within 10 cm^{-1} of the value obtained in the earlier work of Egawa et al.[9a] (510 $\pm$ 3 cm^{-1}) and 50 cm^{-1} from the later work of the same authors[9b] (449 $\pm$ 9 cm^{-1}), the latter obtained using different assumptions regarding the coupling between the various modes. It was therefore suggested in our study that revisiting the analysis of the experimental data might be warranted, especially in lieu of the fact that significant coupling between the ring-puckering angle and CH_2-rocking motions was found. Our previous work has also proposed a procedure for obtaining estimates of the barrier height based on a combination of the results of the cheaper MP2 calculations and the more expensive ones at the CCSD(T) level of theory with smaller basis sets. This was based on the finding that for each set in the family of correlation consistent basis sets, the difference between the MP2 and the CCSD(T) results for the puckering barrier remained constant. We will employ this approach in the current study to theoretically estimate the ring-puckering barrier of c-C_4F_8. Furthermore, we previously presented evidence[12] from natural bond orbital (NBO) analysis[13,14] suggesting that the inversion barrier of C_4H_8 arises from hyperconjugative $\sigma_{CC}\rightarrow\sigma_{CH}^*$ and $\sigma_{CH}\rightarrow\sigma_{CH}^*$ interactions that stabilize the puckered ring geometry. Calculations showed that the barrier vanishes when these interactions are deleted from the electron density, in which case C_4H_8 favors an equilibrium planar geometry. We use the NBO method here to similarly examine the origin of the ring-puckering barrier in C_4F_8 and why the barrier magnitude is considerably smaller than that of C_4H_8.

Early spectroscopy of perfluorocylcobutane (c-C_4F_8) mirrored that of cyclobutane with room-temperature IR and Raman spectra recorded of the gas, liquid, solid, and matrix-isolated phases.[15] However, the smaller rotational constant and an increase in overlapping hot bands made the analysis of the spectra problematic. Although it is generally accepted that c-C_4F_8 has a puckered equilibrium structure of D_{2d} symmetry, there was some debate of this fact 30 years ago. Like c-C_4H_8, a puckered structure of D_{2d} symmetry for c-C_4F_8 should result in 12 IR/Raman coincidences in its fundamental vibrational spectrum whereas these coincidences should be absent in a planar structure of D_{4h} symmetry. Miller and Capwell[8] did in fact observe seven such coincidences in the room-temperature, gas-phase IR and Raman spectra. The fact that not all of the coincidences were observed at room temperature cast some doubt as to the actual symmetry of the equilibrium structure of the molecule. However, this discrepancy may be explained by the fact that if, at room temperature, the puckering inversion barrier is comparable to kT and the reduced mass for the inversion coordinate is large, this will result in puckering levels that are populated above and below the barrier and the spectra would display both D_{4h} and D_{2d} character. This notion is consistent with the fact that electron diffraction measurements[16] of the gas-phase molecule did result in a puckered structure with a dihedral angle of 17.4°.

Harris et al.[17] have previously extrapolated known torsional forces for cyclobutane and 1,1-difluoro-cyclobutane to estimate several possible ring-puckering potentials for perfluorocyclobutane. They also recorded IR and Raman spectra of c-C_4F_8 isolated in an argon matrix at 15 K and observed a sum band at 470 cm^{-1} spaced approximately 30 cm^{-1} above the 444 cm^{-1} fundamental, which they assigned as a 2$\leftarrow$1 sideband transition. In the room-temperature, gas-phase IR spectrum, a sideband at 415 cm^{-1} was also observed; this band disappeared in the reduced temperature matrix spectrum and was consequently assigned as a difference band. On the basis of this 2$\leftarrow$1 splitting and their estimated potentials, Harris et al. concluded that the ring-puckering barrier height is in the vicinity of 124 cm^{-1}.

A previous molecular mechanics calculation by Mao et al.[18] produced a D_{2d} structure for c-C_4F_8 in good agreement with the electron diffraction results. They also reported the force field using a modified Urey−Bradley potential and force constants derived from CF_4 and C_2F_6 as starting points. Their calculated frequencies agree to within about 5% of the measured frequencies, and they provide potential energy distributions with their mode descriptions. The IR-active mode at 1290 cm^{-1}, for example, is described as being 30% CF_2 symmetric stretch and 34% CCC bending. On the basis of their calculations, they reassigned the Raman band at 274 cm^{-1} as having e symmetry rather than the b_2 symmetry assigned to it by Miller and Capwell;[8] their other assignments agree with the ones reported previously.

Fisher et al.[19] reported the barrier heights for c-C_4F_8 to be 70−99 cm^{-1} at the density functional (B3LYP and B3P86) theory, 194 cm^{-1} at the Hartree−Fock, and 490 cm^{-1} at the second-order Møller−Plesset perturbation (MP2) levels of theory. They used the experimentally determined barrier height for c-C_4H_8 to benchmark their results and produced a scaled MP2 value of 320 cm^{-1} as their best estimate for the barrier height of c-C_4F_8. Using this value, they produced a sideband spectrum that shows that most of the sideband intensity is displaced 60 cm^{-1} above and below a fundamental transition with weaker transitions displaced 30 cm^{-1} from the fundamental. They also recorded a jet spectrum of c-C_4F_8 mixed with a helium or argon carrier gas using a FT spectrometer with a resolution of 0.1 cm^{-1}. The spectrum was recorded from 4000 to 400 cm^{-1},

TABLE 1: Optimal Internal Coordinates of the (D_{2d}) Minimum and the (D_{4h}) Transition State of C_4F_8 at Various Levels of Theory[a]

level of theory	basis set	r(C−F$_\alpha$) (Å)	r(C−F$_\beta$) (Å)	r(C−C) (Å)	θ(C−C−C) (deg)	ϕ(F$_\alpha$−C−X) (deg)	χ(F$_\beta$−C−X) (deg)
			D_{2d} minimum				
MP2	cc-pVDZ	1.3469	1.3375	1.5601	88.529	114.051	135.352
	cc-pVTZ	1.3381	1.3286	1.5604	88.866	115.049	134.536
	cc-pVQZ	1.3357	1.3263	1.5608	89.022	115.652	133.937
	aug-cc-pVDZ	1.3546	1.3449	1.5680	89.105	115.932	133.583
	aug-cc-pVTZ	1.3389	1.3298	1.5637	89.071	115.855	133.736
CCSD(T)	cc-pVDZ	1.3473	1.3380	1.5651	88.586	114.274	135.150
	cc-pVTZ	1.3381	1.3288	1.5651	88.928	115.363	134.279
	aug-cc-pVDZ	1.3555	1.3465	1.5738	89.219	116.548	133.004
			D_{4h} transition state				
MP2	cc-pVDZ	1.3419		1.5664		124.713	
	cc-pVTZ	1.3329		1.5654		124.833	
	cc-pVQZ	1.3305		1.5654		124.830	
	aug-cc-pVDZ	1.3494		1.5728		124.825	
	aug-cc-pVTZ	1.3339		1.5683		124.835	
CCSD(T)	cc-pVDZ	1.3424		1.5712		124.724	
	cc-pVTZ	1.3330		1.5699		124.856	
	aug-cc-pVDZ	1.3507		1.5781		124.840	

[a] See Figure 1 for labeling of the atoms.

although they showed no structure below 900 cm^{-1}. This is to be expected since bands below this point are considerably weaker and would be difficult to see in a single pass jet arrangement. They suggested that a band centered at 1150 cm^{-1} may be part of the sideband spectrum of the fundamental centered at 1220 cm^{-1}. Assigning the bands of c-C_4F_8 as fundamental bands, side bands, parallel, perpendicular, etc. is difficult because of the small B value (calculated to be approximately 0.036 cm^{-1}) and the distribution of population over a number of excited ring-puckering states. In the experiment reported by Fisher et al.,[19] it appears that the jet spectrum is not sufficiently cold to reduce hot band structure; in fact, their spectrum did not appear to be all that different from the molecule's room-temperature spectrum. Even if the vibrational temperature were cold enough, they may not have had adequate resolution to resolve any rotational structure.

The previous survey of theoretical and experimental results on c-C_4F_8 clearly warrants further studies on this system. In this study, we report both extensive theoretical ab initio calculations of the structure, harmonic and anharmonic spectra, magnitude and origin of the puckering barrier, and experimental FTIR spectra of the fundamental bands of c-C_4F_8 at moderate resolution (0.1 cm^{-1}) in a room-temperature cell and at high resolution (0.0015 cm^{-1}) for two of the molecule's stronger parallel bands in a slit-jet, supersonic expansion. The theoretical approach for the accurate determination of the structure and the puckering barrier is based on the approach of Dunning and coworkers[20] in utilizing the family of correlation-consistent basis sets to establish the accuracy of the various levels of electronic structure theory of increasing accuracy at the complete basis set (CBS) limit. As noted earlier, the rotational structure of c-C_4F_8 is obscured at room temperature by a large number of hot band transitions. We have observed this in both moderate and high-resolution FTIR spectroscopy of the gas in a room-temperature cell. We have also recorded FTIR spectra between 900 and 1400 cm^{-1} of a slit-jet expansion of the gas mixed in a helium carrier. We estimate the jet temperature to be between 10 and 15 K. We observed two perpendicular and two parallel bands in this region. The two perpendicular bands will be discussed in a subsequent publication. The two parallel fundamental bands at 1292.6 and 1240.3 cm^{-1} are of b_2 symmetry under D_{2d}. The band at 1292.6 cm^{-1}, which is a C−F asymmetric stretch of a_{2u} symmetry under D_{4h}, shows a simple symmetric top spectrum, while the band at 1240.3 cm^{-1}, which is a C−F symmetric stretch and correlates to a b_{1g} symmetry under D_{4h}, shows a single splitting on each rotational transition in the band. We believe that this is due to transitions from the two lowest ring-puckering levels in the ground state to the two lowest ring-puckering states in the first excited state of the fundamental with $+\leftrightarrow-$ puckering selection rules.

II. Experimental and Theoretical Approaches

a. Experiment. The perfluorocyclobutane (CAS #115-25-3) used in these experiments was from Matheson Gas Products and had a stated purity of 99.9%. It was used without further purification. Two series of spectroscopic measurements were made using a Bruker IFS 120HR Fourier transformer spectrometer.

One series of experiments (hereafter referred to as 1a, 1b, and 1c) were of samples of c-C_4F_8 in a static cell with a path length of 19.95 cm. The cell had a jacket surrounding its length that allowed fluid from a constant temperature bath to flow around the cell. For all of the static cell measurements, the cell temperature was maintained at a constant of 25.0 °C. These spectra were recorded with an instrument resolution of 0.1 cm^{-1}. Background spectra were recorded of the empty cell for each experiment. The absorbance spectra were calculated as $-\ln\{I_{sample}/I_{background}\}$. All spectra were recorded with the spectrometer evacuated.

For experiment 1a, the sample pressures of neat c-C_4F_8 were 0.504, 1.06, and 2.10 Torr, the wavenumber range covered was 600−6000 cm^{-1}, and a Globar source and KBr beamsplitter were used along with a liquid nitrogen-cooled HgCdTe detector. Potassium bromide windows were used for the sample cell. For experiment 1b, the neat sample pressures were 1.13, 10.34, 111.82, and 718.18 Torr, the wavenumber range covered was 210−680 cm^{-1}, and a Globar source and KBr beamsplitter were used along with a liquid helium-cooled silicon bolometer detector. KRS-5 windows were used for the sample cell. For experiment 1c, the sample pressure was 29.92 Torr, the wavenumber range covered was 120−370 cm^{-1}, and a mercury arc lamp source and Mylar (3.5 μm thick) beam splitter were used along with a liquid helium-cooled silicon bolometer detector. Silicon windows were used for the sample cell. Spectra were recorded of samples of c-C_4F_8 at various pressures in the

TABLE 2: Vibrationally Averaged Spectroscopic and Structural Constants of C_4F_8 Estimated at the MP2/cc-pVDZ Level of Theory[a]

	MP2/cc-pVDZ	MP2/cc-pVQZ	experiment[b]
$A_z = B_z$ (cm^{-1})	0.035139	(0.03543)	0.03553
$A_e = B_e$ (cm^{-1})	0.035379	0.03567	
C_z (cm^{-1})	0.029069	(0.02898)	0.02880
C_e (cm^{-1})	0.029318	0.02923	
D_J (cm^{-1})	0.95499×10^{-9}		
D_{JK} (cm^{-1})	-0.36970×10^{-9}		
D_K (cm^{-1})	0.22604×10^{-9}		
ZPE (harmonic) (cm^{-1})	10609.4		
ZPE (fundamental) (cm^{-1})	10420.5		
ZPE (anharmonic) (cm^{-1})	10545.3		
r_z(C−C) (Å)	1.567 (+0.007)	(1.568)	1.566 ± 0.008
r_z(C−F) (Å)	1.341 (+0.004)	(1.340)	1.333 ± 0.002
	1.350 (+0.003)	(1.329)	
α_z(F−C−F) (deg)	110.5 (−0.1)	(110.3)	109.9 ± 0.3
θ_z(C−C−C) (deg)	88.6 (+0.1)	(89.1)	89.3 ± 0.3
δ_z(C−C−C−C) (deg)	17.9 (−0.3)	(14.6)	17.4

[a] Subscripts "*e*" and "*z*" denote equilibrium and vibrationally averaged quantities, respectively. The D_J, D_{JK}, and D_K constants correspond to the vibrationally averaged geometry and are computed in the symmetrically reduced Hamiltonian approximation. Numbers in parentheses under the MP2/cc-pVDZ column indicate the effect of vibrational averaging (difference from the MP2/cc-pVDZ equilibrium values) in the structural parameters. Numbers in parentheses under the MP2/cc-pVQZ column indicate the vibrationally averaged estimates when the effect of the correction at the MP2/cc-pVDZ level is added to the equilibrium MP2/cc-pVQZ values. [b] Ref 16.

static cell, at 25.0 °C, and at resolutions on the order of 0.002 cm^{-1}, but none of these showed resolved rotational structure.

The other series of experiments (hereafter referred to as 2a and 2b) were spectra of a molecular beam of *c*-C_4F_8 mixed in helium and expanded through a 12 cm long, 50 μm wide slit into a vacuum chamber. The experiments were performed by steering collimated light out of the interferometer, passing it through a Gregorian telescope to reduce the diameter of the collimated light beam down to a few millimeters, passing that light into the molecular beam expansion chamber, and orthogonally crossing the light with the molecular expansion. The light that left the expansion chamber was focused by a lens and was steered onto a liquid nitrogen-cooled HgCdTe detector. The signal from the detector was fed back into the spectrometer. The spectrometer and telescope chamber were under vacuum when the spectra were recorded. A window separated the telescope and expansion chamber. The optics and detector where the light exited the expansion chamber were surrounded by a plastic bag that was continuously flushed with dry nitrogen to purge room air and water from the optical path. The expansion chamber was pumped by a system of roots blowers and a mechanical vacuum pump that gave a pumping speed of 6000 L/s and a throughput of 600 Torr L/s with an expansion chamber pressure of 0.1 Torr. The *c*-C_4F_8 and helium were flowed from their storage cylinders through separate flow controllers and mixed in the 1/2 in. diameter line leading to the slit jet source. A capacitance manometer on the expansion chamber monitored its pressure.

For experiment 2a, spectra were recorded between 900 and 1400 cm^{-1} at a resolution of 0.0022 cm^{-1}. The spectra were recorded over the course of several days with 180 total single-sided interferograms coadded. Boxcar apodization, a zero-filling factor of 2, a phase resolution of 1 cm^{-1}, and a Mertz phase correction were used for the interferogram transform. The average pressure of *c*-C_4F_8 in the gas line leading to the slit-jet source was 55 Torr with a total average pressure of 574 Torr (including helium). The pressure in the expansion chamber was 0.07 Torr. Background spectra were recorded with no gas flowing through the jet source, and the resolution was set at 0.0320 cm^{-1} and a zero-filling factor of 32. The absorbance spectra were calculated as $-\ln\{I_{sample}/I_{background}\}$. For experiment 2b, spectra were recorded between 1200 and 1300 cm^{-1} at a resolution of 0.0015 cm^{-1}. The spectra were recorded over the course of several days with 90 total single-sided interferograms coadded. Boxcar apodization, a zero-filling factor of 4, a phase

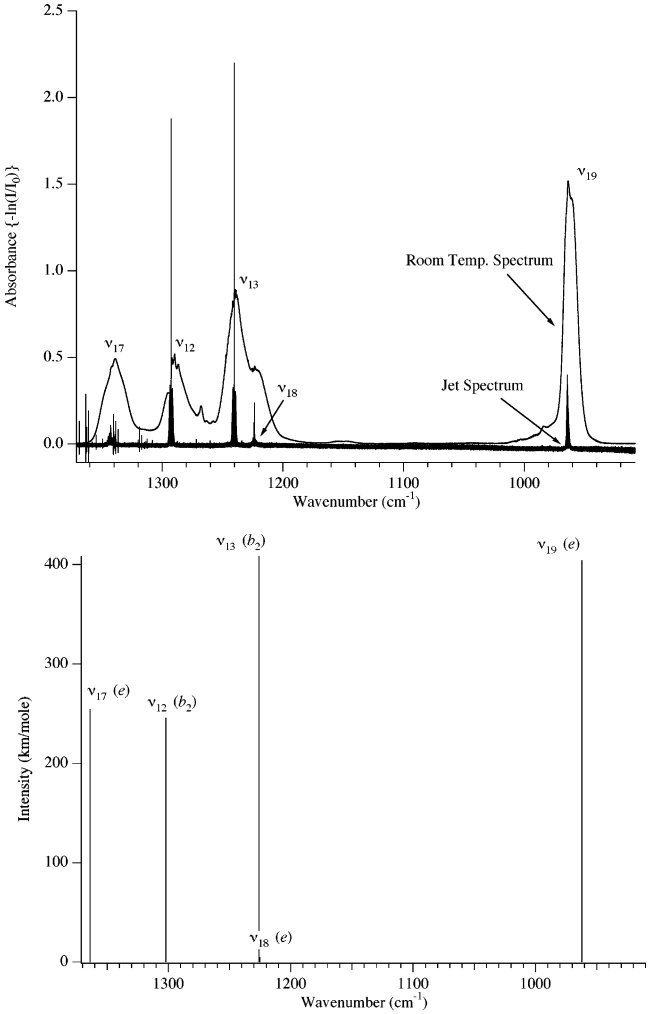

Figure 2. (a) Moderate resolution (0.1 cm^{-1}) room temperature (experiment 1a) and high resolution (0.0022 cm^{-1}) jet (experiment 2a) spectra and (b) IR active MP2/cc-pVTZ calculated anharmonic stick spectrum in the range of 950−1500 cm^{-1}.

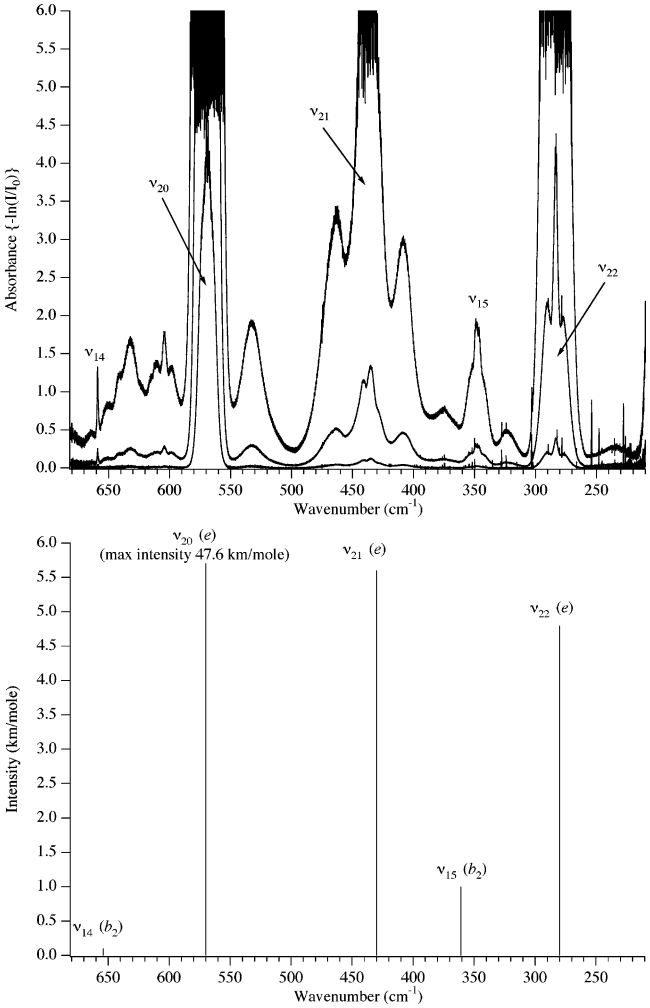

Figure 3. (a) Moderate resolution (0.1 cm^{-1}) spectra for experiment 1b for three different pressures (see text) and (b) IR active MP2/cc-pVTZ calculated anharmonic stick spectrum in the range of 250−700 cm^{-1}.

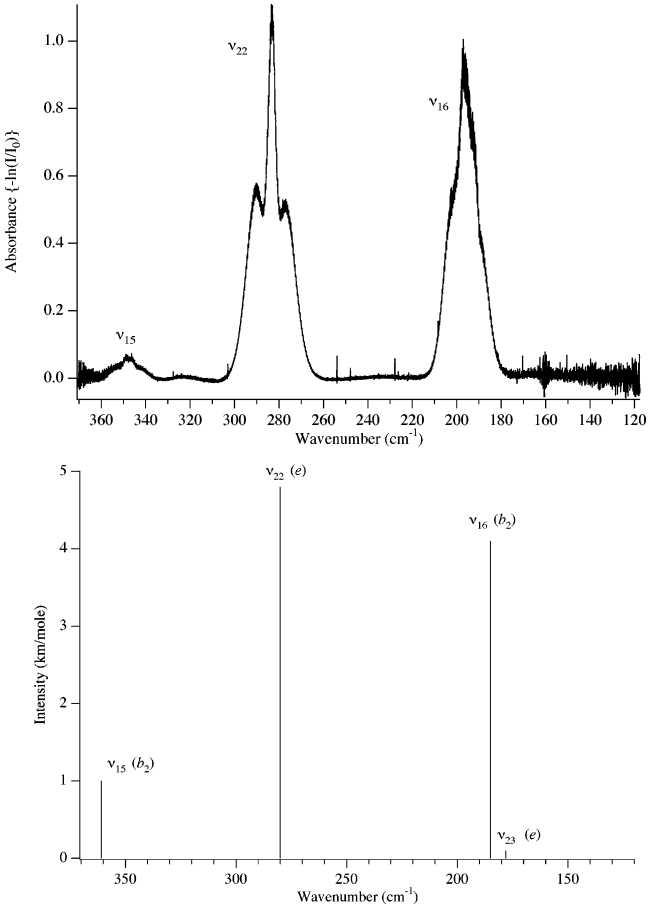

Figure 4. (a) Moderate resolution (0.1 cm^{-1}) spectra for experiment 1c and (b) IR active MP2/cc-pVTZ calculated anharmonic stick spectrum in the range of 120−370 cm^{-1}.

resolution of 1 cm^{-1}, and a Mertz phase correction were used for the interferogram transform. The average pressure of *c*-C_4F_8 in the gas line leading to the slit-jet source was 57 Torr with a total average pressure of 572 Torr (including helium). The pressure in the expansion chamber was 0.07 Torr. Background spectra were recorded with no gas flowing through the jet source, and the resolution was set at 0.0480 cm^{-1} and a zero-filling factor of 128. The absorbance spectra were calculated as $-\ln\{I_{sample}/I_{background}\}$.

To calibrate the wavenumber scale of the jet spectra, a flow of nitrous oxide was expanded through the jet, and the same spectrometer parameters as described in experiment 2b were used to record background and calibration spectra. The wavenumber differences between the recorded nitrous oxide transitions and those found in the NIST reference wavenumber data (http://physics.nist.gov/PhysRefData/wavenum/html/contents.html) were used to calculate an average offset of 0.000589 cm^{-1} that was added to the jet spectrum obtained in experiment 2b.

b. First Principles Electronic Structure Calculations. The geometries of the D_{2d} (minimum) and D_{4h} (transition state) structures (cf. Figure 1) were fully optimized at the second-order MP2 and coupled-cluster singles and doubles with perturbative estimate of triple excitations [CCSD(T)] levels of theory using the family of plain and augmented correlation consistent basis sets, cc-pV*n*Z and aug-cc-pV*n*Z (n = D, T, Q, or 5), respectively.[21]

Geometry optimizations and harmonic frequency analysis using analytic first and second derivatives at the MP2 level of theory were performed with the cc-pVDZ, cc-pVTZ, and aug-cc-pVDZ basis sets, whereas geometry optimizations at the CCSD(T) level of theory were performed numerically with the cc-pVDZ and aug-cc-pVDZ sets. The numerical optimizations were performed using a Z-matrix description of the molecular geometry in terms of the six (D_{2d}) and three (D_{4h}) unique internal coordinates, respectively. Single-point calculations at the optimal geometries (*vide infra*) for each level of theory were performed with the larger basis sets. Anharmonic frequencies[22] and anharmonic vibrational−rotational couplings[23] were computed by numerical differentiation along normal modes at the MP2 level of theory. We followed the approach of Barone, which is based on the second-order perturbation theory and provides closed-form expressions for most of the spectroscopic constants needed for obtaining anharmonic frequencies as implemented in the Gaussian 03[24] suite of programs.

The NBO analysis was applied to density functional theory (DFT) calculations of the planar and puckered geometries of C_4F_8 and C_4H_8. The B3LYP hybrid density functional and the cc-pVDZ basis set were used for this analysis. The B3LYP/cc-pVDZ method yields a smaller puckering barrier (ΔE_e) for C_4F_8 (92 cm^{-1}) than for C_4H_8 (231 cm^{-1}). Although neither barrier at the DFT level compares particularly favorably with the respective CBS values of 132 or 498 cm^{-1} (*vide infra* and ref 11), perturbative analysis of the Kohn−Sham matrix allows for a full exploration of the nature of the individual orbital interactions at the B3LYP level, something that is not possible

TABLE 3: Experimentally Measured and Calculated Anharmonic Frequencies of *c*-C_4F_8

mode no.[a]	D_{2d} species	D_{2d} activity	D_{4h} species	D_{4h} activity	approximate mode description	anharmonic MP2/cc-pVDZ (cm^{-1})	experiment (cm^{-1})
1	a_1	R	a_{1g}	R	ring breathing	1460	1433[b]
2	a_1	R	b_{2u}	inactive	CF_2 antisymmetric str/rock	1286	1413[b]
3	a_1	R	a_{1g}	R	CF_2 symmetric stretch	696	700[b]
4	a_1	R	a_{1g}	R	CF_2 rock	604	607[b]
5	a_1	R	b_{2u}	inactive	CF_2 scissor	365	359[b]
6	a_1	R	b_{2u}	inactive	ring pucker	61	
7	a_2	inactive	a_{2g}	inactive	CF_2 wag	868	
8	a_2	inactive	b_{1u}	inactive	CF_2 twist	208	
9	b_1	R	b_{2g}	R	ring breathing	1035	1010[b]
10	b_1	R	b_{2g}	R	CF_2 wag	272	
11	b_1	R	a_{1u}	inactive	CF_2 twist	242	
12	b_2	R, IR	a_{2u}	IR	CF_2 antisym. str/bend	1302	1292.56039[c]
13	b_2	R, IR	b_{1g}	R	CF_2 sym. stretch	1226	1240.34858[c]
14	b_2	R, IR	b_{1g}	R	mixed	654	658.9[c]
15	b_2	R, IR	b_{1g}	R	CF_2 scissor	360	347.7[c]
16	b_2	R, IR	a_{2u}	IR	CF_2 rock	185	195.0[c]
17	e	R, IR	e_g	R	CF_2 ring breathing	1364	1343.2[c]
18	e	R, IR	e_u	IR	CF_2 antisym. stretch	1225	1223[c]
19	e	R, IR	e_u	IR	CF_2 sym. stretch	962	964.0[c]
20	e	R, IR	e_u	IR	CF_2 scissor	570	569.0[c]
21	e	R, IR	e_g	R	CF_2 rock	430	437.1[c]
22	e	R, IR	e_g	R	CF_2 wag	280	283.2[c]
23	e	R, IR	e_u	IR	CF_2 twist	178	

[a] Mode numbering based on D_{2d} symmetry. [b] Ref 8. [c] Experimentally measured values, this work.

TABLE 4: Calculated Harmonic Frequencies (cm^{-1}) of *c*-C_4F_8[a]

mode	symmetry under D_{2d}	HF cc-pVDZ[b] ω	MP2 cc-pVDZ ω	MP2 aug-cc-pVDZ ω	MP2 cc-pVTZ[c] ω
1	a_1	1635 (2.9)	1495	1461	1485 (0.0)
2	a_1	1455 (1.6)	1320	1265	1314 (0.0)
3	a_1	768 (11.4)	708	689	714 (0.0)
4	a_1	668 (0.8)	613	603	616 (0.0)
5	a_1	396 (2.8)	368	357	369 (0.0)
6	a_1	54 (0.002)	67	46	59 (0.0)
7	a_2	951 (0.0)	880	871	888 (0.0)
8	a_2	233 (0.0)	209	215	215 (0.0)
9	b_1	1185 (7.3)	1059	1045	1042 (0.0)
10	b_1	303 (0.2)	276	275	280 (0.0)
11	b_1	275 (0.8)	245	247	249 (0.0)
12	b_2	1446 (2.0)	1328	1280	1324 (245.8)
13	b_2	1375 (0.4)	1256	1219	1261 (408.6)
14	b_2	720 (0.7)	662	647	667 (0.1)
15	b_2	387 (1.0)	363	348	361 (1.0)
16	b_2	202 (0.002)	185	190	192 (4.1)
17	e	1535 (0.3)	1391	1357	1380 (127.2)
18	e	1377 (1.7)	1248	1200	1245 (2.5)
19	e	1064 (0.03)	980	956	985 (202.2)
20	e	623 (0.02)	576	555	580 (23.8)
21	e	482 (2.2)	434	432	440 (2.8)
22	e	310 (0.04)	283	285	287 (2.4)
23	e	200 (0.03)	180	187	186 (0.1)

[a] Raman scattering activities ($Å^4$/amu) at the HF/cc-pVDZ level and IR intensities (km/mol) at the MP2/cc-pVTZ level are shown in parentheses. [b] Raman scattering activities ($Å^4$/amu) in parentheses computed at the HF/cc-pVDZ level. [c] IR intensities (km/mol) in parentheses computed at the MP2/cc-pVTZ level.

for the MP2 and CCSD(T) methods for which no effective one-electron energy matrix is available.

The largest MP2 calculation was performed with the aug-cc-pV5Z basis set consisting of the segmented contractions [6*s*5*p*4*d*3*f*2*g*1*h*] + (1*s*1*p*1*d*1*f*1*g*1*h*) for the carbon and fluorine atoms for a total of 1524 contracted Gaussian basis functions. The largest CCSD(T) calculation was performed with the cc-pVQZ basis set having a total of 660 contracted Gaussian functions. The calculations were performed with the Gaussian 98 and 03,[24] Molpro,[25] and NWChem[26] suites of codes.

III. Results and Discussion

a. Optimal Geometry. The optimal internal coordinates of the (D_{2d}) minimum and the (D_{4h}) transition state of *c*-C_4F_8 at the various levels of theory considered in this study are listed

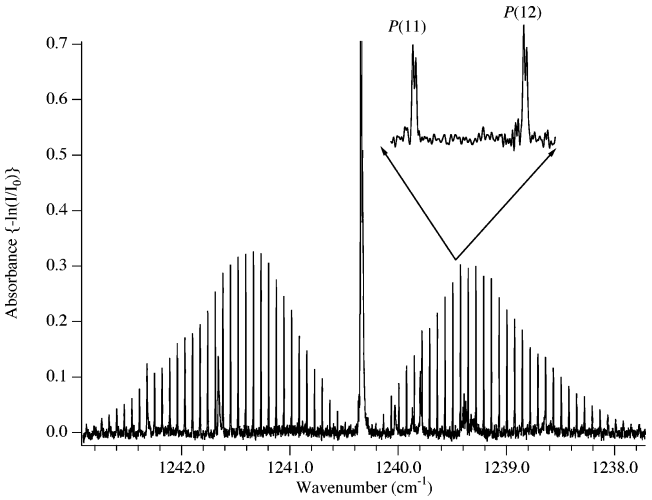

Figure 5. Rovibrational spectrum of the ν_{13} band at 1240.3 cm^{-1}.

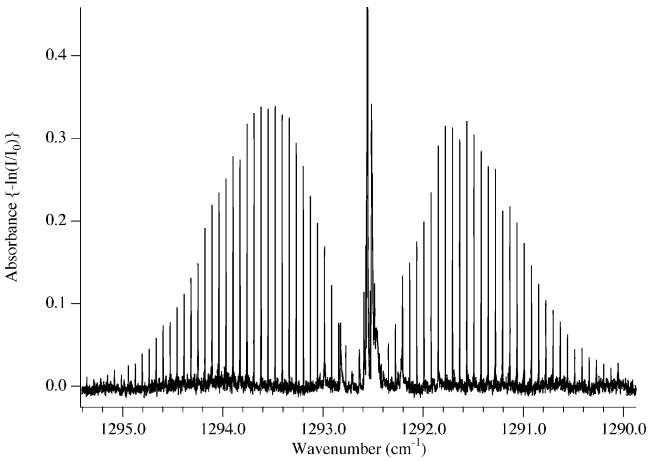

Figure 6. Rovibrational spectrum of the ν_{12} band at 1293.6 cm^{-1}.

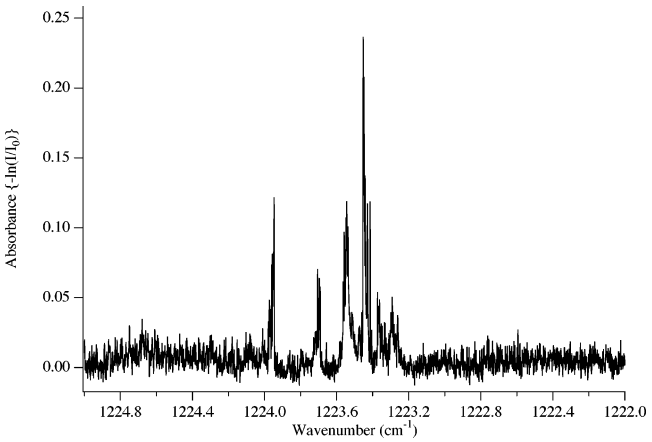

Figure 7. Jet spectrum in the vicinity of 1223 cm^{-1}.

in Table 1. The labeling of the atoms is shown in Figure 1. For the puckered equilibrium structure, there are six degrees of freedom (DOF), whereas for the planar transition state there are only three DOF under D_{4h} symmetry since $r(C-F_\alpha) = r(C-F_\beta)$, $\theta(C-C-C) = 90°$, and $\phi(F_\alpha-C-X) = \phi(F_\beta-C-X)$. The size of the system currently prohibits the use of sets larger than the aug-cc-pVDZ basis for geometry optimizations at the CCSD(T) level of theory and the cc-pVQZ basis for obtaining optimal geometries at the MP2 level of theory. Therefore, single-point energy calculations have been performed at the best geometries for each level of theory in order to arrive at an accurate value for the ring-puckering barrier (see section III.c below).

TABLE 5: Rovibrational Transition Frequencies of the ν_{13} Parallel Band (1240.3 cm^{-1}), Strong Component

assignment	frequency	observed − calculated	assignment	frequency	observed − calculated
P(30)	1238.20859	0.000427	*R*(2)	1240.56128	0.000280
P(29)	1238.27986	−0.000127	*R*(3)	1240.63178	0.000040
P(28)	1238.35187	0.000092	*R*(4)	1240.70257	0.000123
P(27)	1238.42337	−0.000166	*R*(5)	1240.77315	0.000029
P(26)	1238.49525	−0.000011	*R*(6)	1240.84377	0.000008
P(25)	1238.56677	−0.000183	*R*(7)	1240.91434	−0.000030
P(24)	1238.63871	0.000098	*R*(8)	1240.98487	−0.000076
P(23)	1238.71095	0.000711	*R*(9)	1241.05545	−0.000039
P(22)	1238.78154	−0.000292	*R*(10)	1241.12600	0.000001
P(21)	1238.85346	0.000067	*R*(11)	1241.19643	−0.000046
P(20)	1238.92481	−0.000111	*R*(12)	1241.26692	0.000000
P(19)	1238.99629	−0.000126	*R*(13)	1241.33733	−0.000001
P(18)	1239.06776	−0.000118	*R*(14)	1241.40778	0.000070
P(17)	1239.13919	−0.000118	*R*(15)	1241.47811	0.000055
P(16)	1239.21056	−0.000144	*R*(16)	1241.54833	−0.000038
P(15)	1239.28202	−0.000048	*R*(17)	1241.61872	0.000072
P(14)	1239.35332	−0.000079	*R*(18)	1241.68889	−0.000005
P(13)	1239.42461	−0.000087	*R*(19)	1241.75891	−0.000200
P(12)	1239.49582	−0.000142	*R*(20)	1241.82952	0.000229
P(11)	1239.56704	−0.000155	*R*(21)	1241.89950	0.000060
P(10)	1239.6383	−0.000094	*R*(22)	1241.96967	0.000114
P(9)	1239.70948	−0.000081	*R*(23)	1242.03954	−0.000099
P(8)	1239.78059	−0.000105	*R*(24)	1242.10988	0.000191
P(7)	1239.85169	−0.000106	*R*(25)	1242.17936	−0.000346
P(6)	1239.92279	−0.000074	*R*(26)	1242.24967	−0.000020
P(5)	1239.99397	0.000071	*R*(27)	1242.31948	−0.000162
P(4)	1240.06510	0.000198	*R*(29)	1242.45950	0.000053
P(3)	1240.13603	0.000158			
P(2)	1240.20709	0.000282			

TABLE 6: Rovibrational Transition Frequencies of the ν_{13} Parallel Band (1240.3 cm^{-1}), Weak Component

assignment	frequency	observed − calculated	assignment	frequency	observed − calculated
P(30)	1238.20559	−0.000013	*R*(2)	1240.55898	−0.000170
P(29)	1238.27713	−0.000343	*R*(3)	1240.62984	−0.000045
P(28)	1238.34892	−0.000389	*R*(4)	1240.70038	−0.000205
P(27)	1238.42134	0.000229	*R*(5)	1240.77108	−0.000170
P(26)	1238.49271	−0.000168	*R*(6)	1240.84170	−0.000181
P(25)	1238.56447	−0.000141	*R*(7)	1240.91228	−0.000198
P(24)	1238.63613	−0.000179	*R*(8)	1240.98296	−0.000080
P(23)	1238.70806	0.000087	*R*(9)	1241.05372	0.000152
P(22)	1238.77973	0.000127	*R*(10)	1241.12409	0.000029
P(21)	1238.85168	0.000482	*R*(11)	1241.19464	0.000120
P(20)	1238.92297	0.000212	*R*(12)	1241.26514	0.000195
P(19)	1238.99464	0.000356	*R*(13)	1241.33549	0.000155
P(18)	1239.06612	0.000344	*R*(14)	1241.40597	0.000279
P(17)	1239.13748	0.000247	*R*(15)	1241.47628	0.000268
P(16)	1239.20878	0.000124	*R*(16)	1241.54683	0.000531
P(15)	1239.28031	0.000265	*R*(17)	1241.61700	0.000449
P(14)	1239.35148	0.000081	*R*(18)	1241.68693	0.000161
P(13)	1239.42284	0.000122	*R*(19)	1241.75714	0.000187
P(12)	1239.49414	0.000136	*R*(20)	1241.82728	0.000178
P(11)	1239.56526	0.000006	*R*(21)	1241.89721	−0.000007
P(10)	1239.63633	−0.000141	*R*(22)	1241.96725	−0.000047
P(9)	1239.70753	−0.000123	*R*(23)	1242.03722	−0.000123
P(8)	1239.77855	−0.000250	*R*(24)	1242.10731	−0.000044
P(7)	1239.84972	−0.000193	*R*(25)	1242.17696	−0.000371
P(6)	1239.92090	−0.000092	*R*(26)	1242.24688	−0.000394
P(5)	1239.99192	−0.000116	*R*(27)	1242.31713	−0.000052
P(4)	1240.06282	−0.000226	*R*(29)	1242.45684	−0.000055
P(3)	1240.13365	−0.000371			
P(2)	1240.20433	−0.000632			

For the C−F bond lengths, the difference between MP2 and CCSD(T) amounts to <0.0005 Å (cc-pVDZ) and <0.0015 Å (aug-cc-pVDZ). For the C−C bond lengths, this difference is larger (0.005 Å), especially for the planar D_{4h} configuration. The corresponding differences between MP2 and CCSD(T) for the bond angles are <0.3° (cc-pVDZ set). As a general trend, the C−F bond lengths of the minimum configuration contract when the size of the basis set is increasing (i.e., going from the

TABLE 7: Rovibrational Transition Frequencies of the ν_{13} (1292.6 cm^{-1}) Parallel Band

assignment	frequency	observed − calculated	assignment	frequency	observed − calculated
P(35)	1290.05293	0.000004	*R*(1)	1292.70185	−0.000073
P(34)	1290.12529	−0.000042	*R*(2)	1292.77259	−0.000070
P(33)	1290.19757	−0.000124	*R*(3)	1292.84322	−0.000132
P(32)	1290.26994	−0.000070	*R*(4)	1292.91388	−0.000119
P(31)	1290.34226	−0.000022	*R*(5)	1292.98461	0.000009
P(30)	1290.41426	−0.000248	*R*(6)	1293.05514	−0.000018
P(29)	1290.48669	0.000001	*R*(7)	1293.12563	−0.000040
P(28)	1290.55885	0.000025	*R*(8)	1293.19608	−0.000056
P(27)	1290.63103	0.000114	*R*(9)	1293.26650	−0.000058
P(26)	1290.70311	0.000149	*R*(10)	1293.33689	−0.000044
P(25)	1290.77513	0.000168	*R*(11)	1293.40730	0.000035
P(24)	1290.84704	0.000123	*R*(12)	1293.47763	0.000079
P(23)	1290.91890	0.000072	*R*(13)	1293.54791	0.000118
P(22)	1290.99074	0.000047	*R*(14)	1293.61812	0.000132
P(21)	1291.06255	0.000037	*R*(15)	1293.68823	0.000091
P(20)	1291.13433	0.000042	*R*(16)	1293.75836	0.000116
P(19)	1291.20608	0.000062	*R*(17)	1293.82842	0.000115
P(18)	1291.27778	0.000077	*R*(18)	1293.89845	0.000130
P(17)	1291.34939	0.000048	*R*(19)	1293.96836	0.000070
P(16)	1291.42104	0.000103	*R*(20)	1294.03830	0.000085
P(15)	1291.49259	0.000104	*R*(21)	1294.10821	0.000115
P(14)	1291.56407	0.000079	*R*(22)	1294.17807	0.000140
P(13)	1291.63550	0.000050	*R*(23)	1294.24788	0.000160
P(12)	1291.70683	−0.000034	*R*(24)	1294.31756	0.000095
P(11)	1291.77812	−0.000113	*R*(25)	1294.38721	0.000046
P(10)	1291.84943	−0.000126	*R*(26)	1294.45681	−0.000009
P(9)	1291.92073	−0.000105	*R*(27)	1294.52637	−0.000058
P(8)	1291.99202	−0.000049	*R*(28)	1294.59580	−0.000192
P(7)	1292.06321	−0.000047	*R*(29)	1294.66543	−0.000081
P(6)	1292.13439	−0.000010	*R*(30)	1294.73488	−0.000105
P(5)	1292.20541	−0.000089	*R*(31)	1294.80427	−0.000144
P(4)	1292.27648	−0.000072	*R*(32)	1294.87365	−0.000147
P(3)	1292.34735	−0.000210	*R*(33)	1294.94319	0.000054
P(2)	1292.41833	−0.000193	*R*(34)	1295.01242	−0.000009
			R(35)	1295.08169	0.000012

cc-pVDZ to the cc-pVQZ set), whereas the inclusion of additional diffuse functions in the basis set (cc-pVDZ vs aug-cc-pVDZ) has an effect in the opposite direction. The results of Table 1 indicate that the geometry is converged with the triple-ζ quality set as there are minimal changes (<0.003 Å, <0.4°) upon reoptimization with the larger cc-pVQZ set.

The effects of vibrational averaging on the structure of C_4F_8 at the MP2/cc-pVDZ level are shown in Table 2, where subscripts "*e*" and "*z*" denote equilibrium and vibrationally averaged values, respectively. The magnitude and sign of the vibrational corrections on the structural parameters (differences between the equilibrium and vibrationally averaged structure at the MP2/cc-pVDZ level of theory) are indicated in parentheses in Table 2 under the MP2/cc-pVDZ column. If the MP2/cc-pVDZ vibrational corrections are applied to the MP2/cc-pVQZ equilibrium geometries, the resulting MP2/cc-pVQZ vibrationally corrected rotational constants and structural parameters (in parentheses under the corresponding column in Table 2) are in excellent agreement (within the experimental error bars) with the previously determined values from electron diffraction studies except for the (C−C−C−C) dihedral angle δ_z. Interestingly, in these previous studies, the two C−F bond lengths were assigned the same value with an error bar of ±0.002 Å, a value that is an order of magnitude smaller than the calculated difference (~0.010 Å) between $r(C-F_\alpha)$ and $r(C-F_\beta)$, as shown in Table 1. This might explain the fact that the set of MP2/cc-pVQZ corrected vibrationally averaged r_z-(C−F) bond lengths brackets the single experimental value.

b. Vibrational Frequencies. The moderate resolution (0.1 cm^{-1}) spectra for experiments 1a, 1b, and 1c are shown in Figures 2a, 3a, and 4a, respectively. The mode number, its symmetries under D_{2d} and D_{4h}, its approximate description, and the assigned experimental and calculated anharmonic frequencies (at the MP2/cc-pVDZ level of theory) are given in Table 3. The corresponding MP2/cc-pVDZ anharmonic fundamental spectra are shown in Figures 2b, 3b, and 4b. Furthermore, the harmonic frequencies and their IR intensities with different basis sets at the MP2 level together with Raman scattering activities (Å^4/amu) computed at the HF/cc-pVDZ level are given in Table 4. The fundamental mode numbering is based on D_{2d} symmetry and is given in accordance with the current IUPAC standard; it is consistent with the one previously given by Mao et al.[18] and Fisher et al.[19] Because we did not record the Raman spectrum of the molecule, the fundamental ν_1 to ν_5 and ν_9 frequencies reported in Table 3 are the gas-phase values originally recorded and assigned by Miller and Capwell.[8] The ring-puckering mode, ν_6, has not been observed, the ν_7 and ν_8 modes are inactive, and the ν_{10} and ν_{11} modes are weak.

At room temperature, we observed 10 of the 12 IR-active fundamental bands at moderate resolution (0.1 cm^{-1}). The four strongest IR-absorbing modes are found between 900 and 1400 cm^{-1}. On the basis of the first jet spectra that we recorded (experiment 2a; resolution, 0.0022 cm^{-1}), it is clear that the bands at 1292.6 (ν_{12}) and 1240.3 cm^{-1} (ν_{13}) are parallel bands and the bands at 1343.2 (ν_{17}) and 964 cm^{-1} (ν_{19}) are perpendicular bands (see also Figure 2a). The rovibrational transitions in the ν_{13} band appeared to be broader than those in the ν_{12} band, and selection rules for the ν_{13} band suggest that it may be possible to observe a torsional tunneling splitting for each of the band's rovibrational lines, so we recorded the ν_{12} and ν_{13} bands again at the spectrometer's ultimate resolution of 0.0015 cm^{-1} (experiment 2b). These bands are shown in Figures 5 and 6, respectively. The corresponding rovibrational spectra for the ν_{17} and ν_{19} bands at higher resolutions and better signal-to-noise ratios will be presented elsewhere. The calculations predict that the weak ν_{18} perpendicular band should lie in the region near 1223 cm^{-1} as well. We do observe in the jet spectrum a group of what appear to be *Q*-branches in the vicinity of 1223 cm^{-1}, as seen in Figure 7. Some of these *Q*-branches may belong to a tunneling sideband structure, and one may belong to ν_{18}, but with the present signal-to-noise, it is not possible to make a definitive assignment.

The remaining IR-active fundamental modes appear below 700 cm^{-1}. For experiment 1b, the results between 210 and 680 cm^{-1} are also shown in Figure 3a for pressures 29.92, 111.82, and 718.18 Torr, respectively. The ν_{14} band is very weak and gains appreciable intensity in the 20 cm, room-temperature cell only at pressures above 100 Torr. The *Q*-branch for this band of b_2 symmetry is centered at 658.9 cm^{-1}. The three perpendicular bands in this window, ν_{20}, ν_{21}, and ν_{22}, are centered at 569.0, 437.1, and 283.2 cm^{-1}, respectively. These bands show side lobes, and at first, it may be tempting to assign these as *P*- and *R*-branch rotational structures. However, at room temperature, the *P*- and *R*-branches for a parallel band of *c*-C_4F_8 with a ground state *B* value of 0.03544 cm^{-1} would peak at about $J = 55$, which is displaced by 4 cm^{-1} from the band center. The side lobes of these bands are displaced by more than 4 cm^{-1} from the band center. The peaks of the side lobes for the ν_{22} mode at 283.2 cm^{-1} are displaced by about 8 cm^{-1} from the band center. In all likelihood, these lobes are ring-puckering side band structures. The ν_{15}, b_2 symmetry band also appears in this window and is centered at 347.7 cm^{-1}.

The recorded spectra for experiment 1c are shown in Figure 4a. This window overlaps with that shown in Figure 3a, covering the range from 370 to 120 cm^{-1}. Again, the ν_{15} and ν_{22}

TABLE 8: Fitted Spectroscopic Constants for the ν_{12} and ν_{13} Bands of *c*-C_4F_8.

	ν_{13} band			
	strong component	weak component	ν_{12} band	MP2/cc-pVQZ this work
ν_0	1240.34858(4)	1240.34674(5)	1292.56031(2)	1226 (ν_{13}) 1302 (ν_{12})
B'	0.0354192(7)	0.0354188(9)	0.0354137(3)	0.03543
B''	0.0354355(7)	0.0354360(9)	0.0354363(3)	
rms (o − c)	0.000175	0.000246	0.000101	

TABLE 9: Energies of the (D_{2d}) Minimum and the (D_{4h}) Transition State and Their Energy Separation at Various Levels of Theory[a]

level of theory	basis set	geometry used	E (D_{2d}) (a.u.)	E (D_{4h}) (a.u.)	ΔE_e (cm^{-1})	$\Delta\Delta E_e$ [MP2-CCSD(T)] (cm^{-1})
MP2	cc-pVDZ	optimized	−948.950501	−948.947933	**563.6**	
	cc-pVTZ	cc-pVDZ	−949.886068	−949.884586	325.3	
		optimized	−949.886788	−949.885208	**346.8**	
	cc-pVQZ	cc-pVDZ	−950.188278	−950.187307	213.1	
		cc-pVTZ	−950.189400	−950.188233	256.1	
		optimized	−950.189469	−950.188274	**262.3**	
	cc-pV5Z	cc-pVTZ	−950.304389	−950.303489	197.5	
		cc-pVQZ	−950.304496	−950.303547	**208.3**	
	CBS(cc-pV*n*Z) limit				**176 ± 19**[c]	
	aug-cc-pVDZ	optimized	−949.183784	−949.182968	179.1	
	aug-cc-pVTZ	aug-cc-pVDZ	−949.962982	−949.961903	236.8	
		optimized	−949.964450	−949.963456	**218.2**	
	aug-cc-pVQZ	aug-cc-pVDZ	−950.221137	−950.220195	206.7	
		aug-cc-pVTZ	−950.223614	−950.222721	**196.0**	
	aug-cc-pV5Z	aug-cc-pVDZ	−950.317348	−950.316466	193.6	
		aug-cc-pVTZ	−950.319966	−950.319098	**190.5**	
	CBS(aug-cc-pV*n*Z) limit				**189**[c]	
CCSD(T)	cc-pVDZ	optimized	−949.026809	−949.024538	**498.4**	65.2
	cc-pVTZ	cc-pVDZ	−949.980921	−949.979655	277.9	47.4
		optimized	−949.981700	−949.980343	**297.8**	48.9
	cc-pVQZ	cc-pVDZ	−950.278382	−950.277636	163.7	49.4
		cc-pVTZ	−950.279608	−950.278665	**207.0**	**49.2**
	cc-pV5Z				**(159.1)**[b]	
	CBS(cc-pV*n*Z) limit				**120 ± 6**[c]	
	aug-cc-pVDZ	optimized	−949.275316	−949.274734	127.7	51.4
	aug-cc-pVTZ	aug-cc-pVDZ	−950.062343	−950.061501	**184.8**	**52.0**
	aug-cc-pVQZ				**(154.7)**[b]	
	aug-cc-pV5Z				**(141.6)**[b]	
	CBS(aug-cc-pV*n*Z) limit				**132**[c]	

[a] Bold entries denote the best estimate for the puckering barrier (ΔE_e) at the corresponding level of theory and basis set. [b] Estimated from MP2 assuming that the difference $\Delta(\Delta E_e)$ between MP2 and CCSD(T) is independent of the basis set; see text. [c] Exponential extrapolation.

fundamental modes are shown. The ν_{16} fundamental mode of b_2 symmetry is centered at approximately 195.0 cm^{-1}. The ν_{23} mode should appear in this region, but it is predicted to be weak and may be buried under the ν_{16} band or lost in the noise below 180 cm^{-1}. No further attempt was made to locate ν_{23}.

The calculated MP2/cc-pVDZ anharmonic frequencies (listed in Table 3) are in satisfactory agreement with the measured experimental fundamentals. For the calculated anharmonic frequencies, except ν_2, the largest difference $|\nu_{calcd} - \nu_{exp}|$ is 27 cm^{-1} for the ν_1 mode, whereas for the other ones it is <15 cm^{-1} and in some cases <5 cm^{-1}. The exception is ν_2, for which the difference is 127 cm^{-1}, a value well outside the range for all others. This comparison seems to cast some doubt with regard to the experimental assignment of the Raman active ν_2 band at 1413 cm^{-1}.[8] The fact that the MP2/cc-pVDZ anharmonic frequencies are in satisfactory agreement with the observed IR spectrum both in the band positions and in the relative intensities is also evident from Figures 2−4.

The ν_{13} and ν_{12} modes are both parallel bands, and the expanded views of the jet spectra (experiment 2b) are shown in detail in Figures 5 and 6, respectively. The *P*- and *R*-branches of both bands peak at about $J'' = 13$, and we estimate the rotational temperature of *c*-C_4F_8 in the jet at about 15 K. The full width at half-maximum (fwhm) of the rovibrational transitions of ν_{12} is 0.00220 cm^{-1}, and transitions up to $J'' = 35$ were measured. Assignment of the ν_{13} band is straightforward and is given in Tables 5 and 6. To fit the band, a simple rigid rotor model was used in which the band center and upper and lower state rotational constants were fit. Attempts at fitting quartic centrifugal distortion constants were unsuccessful; the distortion constants were indeterminate in the fit. Fitting the 69 transitions with three constants results in a fit with a root-mean-square observed minus calculated of 0.000101 cm^{-1}. The results of the fit are summarized in Table 7. The ν_{12} mode is of b_2 symmetry under D_{2d} as are all of the other IR-active modes for *c*-C_4F_8. This symmetry species correlates to a_{2u} symmetry under D_{4h} and consequently has $\pm \leftarrow \pm$ ring-puckering selection rules and transitions from the ground state, and occupied excited torsional states should overlap at the resolution studied here.

At an instrument resolution of 0.0015 cm^{-1}, each of the rovibrational transitions of the ν_{13} band show a splitting of approximately 0.0018 cm^{-1} (see Figure 5). Again, this mode is of b_2 symmetry under D_{2d} but correlates to b_{2g} under D_{4h}. In this case, the ring-puckering selection rules are $\pm \leftarrow \mp$ and transitions from the ground and first excited torsional states will be separated by the torsional splitting in the ground and excited

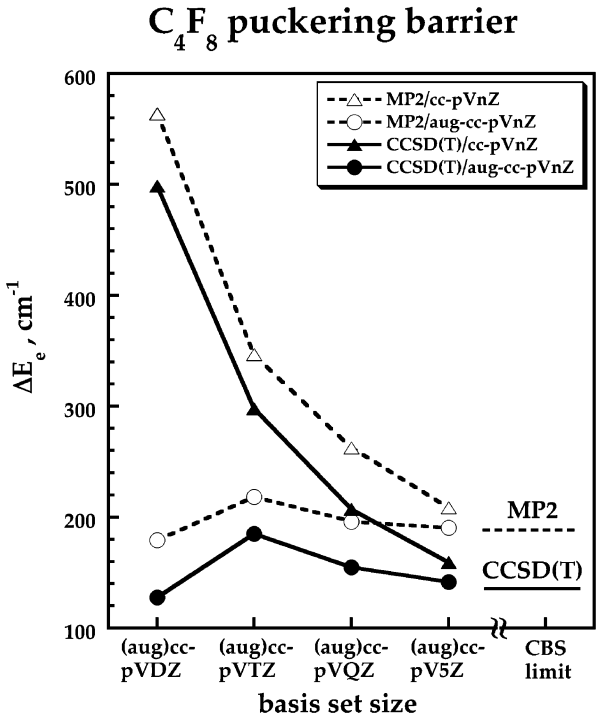

Figure 8. Variation of the ring-puckering barrier (in cm^{-1}) with basis set at the MP2 (open symbols) and CCSD(T) (filled symbols) levels of theory. The *x*-axis corresponds to the cardinal number of the cc basis sets ($n = 2$, 3, 4, and 5 for DZ, TZ, QZ, and 5Z, respectively). Triangles trace the results with the plain (cc-pV*n*Z) basis sets, whereas circles denote the ones with the augmented (aug-cc-pV*n*Z) basis sets.

TABLE 10: NBO Analysis of the Key Hyperconjugative Interactions in Planar (D_{4h}) and Puckered (D_{2d}) Geometries of C_4F_8 and C_4H_8[a]

interactions	D_{4h}	interactions	D_{2d}
	C_4F_8		
$\sigma_{CC}\rightarrow\sigma_{CF}^*(16)$	553	$\sigma_{CC}\rightarrow\sigma_{\beta}^*(8)$	1028
		$\sigma_{CC}\rightarrow\sigma_{\alpha}^*(8)$	213
$\sigma_{CF}\rightarrow\sigma_{CF}^*(16)$	199	$\sigma_{\alpha}\rightarrow\sigma_{\alpha}^*(8)$	304
		$\sigma_{\beta}\rightarrow\sigma_{\beta}^*(8)$	119
ΣE^b	12032		13312
	C_4H_8		
$\sigma_{CH}\rightarrow\sigma_{CH}^*(16)$	518	$\sigma_{CC}\rightarrow\sigma_{\beta}^*(8)$	1207
		$\sigma_{CC}\rightarrow\sigma_{\alpha}^*(8)$	94
$\sigma_{CH}\rightarrow\sigma_{CH}^*(16)$	423	$\sigma_{\alpha}\rightarrow\sigma_{\alpha}^*(8)$	825
		$\sigma_{\beta}\rightarrow\sigma_{\beta}^*(8)$	157
ΣE^b	15056		18264

[a] All values (in cm^{-1}) are second-order estimates of interaction strengths from perturbative analysis of the B3LYP/cc-pVDZ Kohn−Sham matrix. σ_{α}^* and σ_{β}^*, respectively, refer to the axial and equatorial C−F or C−H antibonds. Values in parentheses indicate the number of interactions of that type. [b] Sum of interaction energies.

vibrational states. For each pair of split transitions, the transition to higher wavenumber is the more intense transition and the transition on the low wavenumber side is 10−20% weaker. To fit the data, we treated the strong and weak transtions as two separate bands, and as with the ν_{12} mode, we used a simple rigid rotor model to fit the band center and upper and lower state rotational constants for each of these. The results for the rotational constant, shown in Table 8, are in excellent agreement (within 0.00002 cm^{-1}) with the vibrationally averaged MP2/cc-pVQZ corrected value presented earlier in section III.a and listed in Table 2. The measured ν_{12} and ν_{13} fundamentals are within 9.5 and 14.5 cm^{-1} from the MP2/cc-pVDZ anharmonic frequencies, respectively (see also Table 3). Again, attempts of fitting the distortion constants for these bands were unsuccessful, but fitting the three constants for the strong and weak bands resulted in RMS (observed − calculated) values of 0.000175 and 0.000246 cm^{-1}, respectively. Each band has 56 transitions assigned with maximum $J'' = 30$ on the *P*-branch side and $J'' = 29$ on the *R*-branch side.

c. Magnitude of the Ring-Puckering Barrier. Following the approach we have adopted earlier[11] for C_4H_8, we have systematically examined the effect of the following three factors on the magnitude of the ring-puckering barrier: (i) level of electron correlation, (ii) size of orbital basis set, and (iii) geometry.

The first is examined at the MP2 and CCSD(T) levels of theory wherein the family of correlation-consistent basis sets provides a vehicle for estimating the CBS limits of the barriers for these two methods. The energies of the minimum (D_{2d}) and transition state (D_{4h}) configurations (in a.u.) and the magnitude of the puckering barrier, ΔE_e (in cm^{-1}), are listed in Table 9. The variation of the barrier with basis set size and the corresponding CBS limits at the MP2 and CCSD(T) levels of theory is shown in Figure 8. For each combination of method/basis set, the bold entries in that table denote the "best result" (calculated or estimated) for the puckering barrier. The calculation of the barrier at a particular level of theory/basis set using geometries optimized with smaller basis sets is a measure of the effect of the geometry on that quantity. For example, at the MP2 level of theory, the effect of using the cc-pVQZ optimal geometry as opposed to the cc-pVDZ geometry can be as large as ∼50 cm^{-1} or about 20%. This effect is smaller when using the optimal geometries determined with the family of augmented sets. The CBS limit for the barrier height at the MP2 level of theory is estimated at 176 ± 19 (cc-pV*n*Z, $n = 2-5$) and 189 cm^{-1} (aug-cc-pV*n*Z, $n = 3-5$) following the previously proposed heuristic extrapolation scheme that is based on an exponential variation[27] of the barrier height with the cardinal number of the basis set *n*. The values indicated in bold face in Table 9 are used for the exponential extrapolation. It should be emphasized that our best estimate for the MP2/CBS(aug-cc-pV*n*Z) barrier height of 189 cm^{-1} differs by less than 1.5 cm^{-1} away from the best computed value at the MP2/aug-cc-pV5Z//MP2/aug-cc-pVTZ level of theory.

To estimate the CBS limit at the CCSD(T) level of theory, we rely on the observation made in our previous study[11] of C_4H_8 that for a particular basis set the difference between the MP2 and the CCSD(T) barrier heights remains constant. This is graphically shown in Figure 8, in which the broken lines tracing the MP2 results are almost parallel to the continuous lines tracing the CCSD(T) results. This difference (in cm^{-1}) for C_4F_8 is also shown in Table 9 where the reference geometries are kept the same for consistency. For example,

$$\Delta\Delta E_e(\gamma//\delta)\ [\text{MP2-CCSD(T)}] = \Delta E_e(\text{MP2}/\gamma//\text{MP2}/\delta) - \Delta E_e[\text{CCSD(T)}/\gamma//\text{CCSD(T)}/\delta]$$

where γ, δ refer to different basis sets and the notation MP2/γ//MP2/δ indicates a single point calculation at the MP2 level with basis set γ using the geometry obtained at the MP2 level with basis set δ. We observe that this difference converges to ∼49 cm^{-1} for the plain sets and 52 cm^{-1} for the augmented sets. We therefore use these values to estimate the CCSD(T)/cc-pV5Z, CCSD(T)/aug-cc-pVQZ, and CCSD(T)/aug-cc-pV5Z barrier heights (shown in parentheses in boldface in Table 9) from the corresponding MP2 results with the same basis sets. CCSD(T)/CBS limits of 120 ± 6 (cc-pV*n*Z, $n = 2-5$) and 132 cm^{-1} (aug-cc-pV*n*Z,$n = 3-5$) are then obtained by exponential

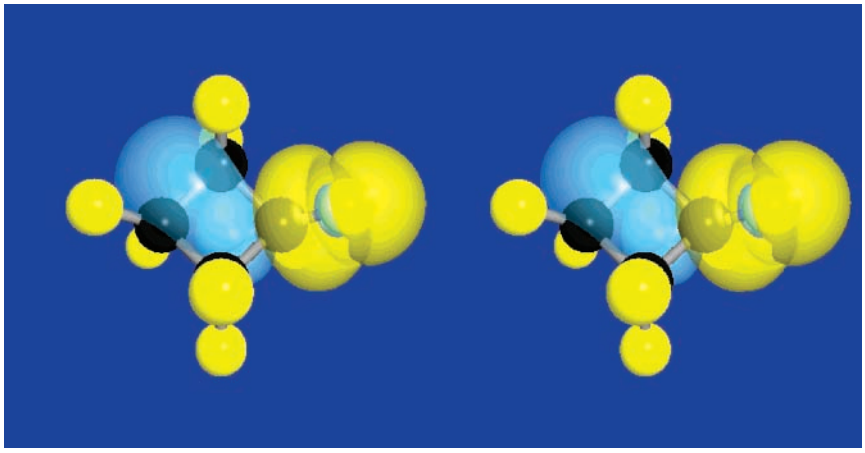

Figure 9. Stereoview of the $\sigma_{CC} \rightarrow \sigma_{\beta}^*$ interaction in puckered C_4F_8. The centroid of the strained C−C bond (between the upper left Carbon atoms) is somewhat shifted to the outside of the ring. The bond overlaps the backside lobe of the C−F antibond in the interior of the ring. The blue and yellow colors, respectively, represent the positive and negative phases of the orbitals.

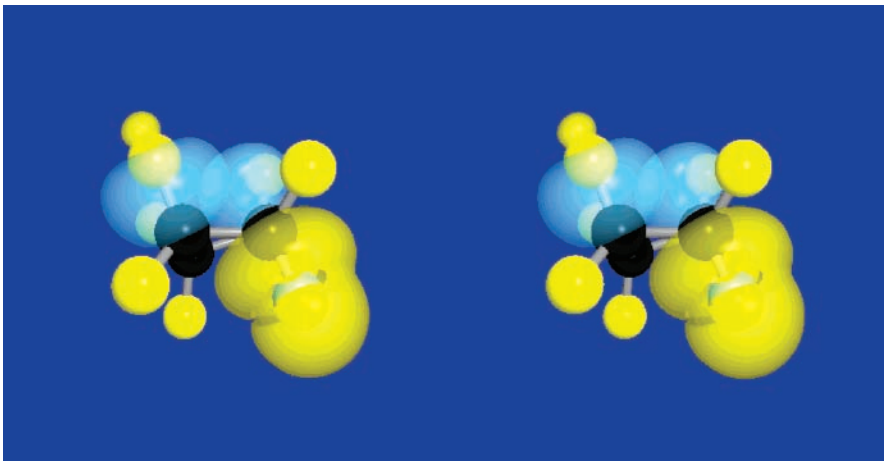

Figure 10. Stereoview of an axial−axial $\sigma_{\alpha} \rightarrow \sigma_{\alpha}^*$ interaction in puckered C_4F_8. The C−F bond of the left-hand carbon weakly overlaps the backside lobe of the C−F antibond of the right-hand carbon. The blue and yellow colors, respectively, represent the positive and negative phases of the orbitals.

extrapolation as in the case for MP2. Hence, our best estimate for the ring-puckering barrier at the CCSD(T)/CBS level of theory is 132 cm^{-1}. This is about one-quarter of the corresponding theoretical estimate for the barrier for C_4H_8 obtained in a similar manner. The agreement of the theoretical estimate for C_4H_8 with experiment lends credibility to our barrier result for C_4F_8, which has not yet been measured experimentally.

d. Origin of the Ring-Puckering Barrier. To investigate the origin of the puckering barrier, we focus our discussion on the key orbital couplings (hyperconjugative interactions) in C_4F_8 that most strongly influence ring puckering. Table 10 lists second-order perturbative estimates of the strengths of these key interactions for the B3LYP/cc-pVDZ densities. Two interaction types are considered, those of the C−C bonds with vicinal C−F antibonds ($\sigma_{CC} \rightarrow \sigma_{CF}^*$) and those of the C−F bonds with *trans* C−F antibonds ($\sigma_{CF} \rightarrow \sigma_{CF}^*$). The planar geometry of C_4F_8 exhibits 16 equivalent $\sigma_{CC} \rightarrow \sigma_{CF}^*$ interactions and 16 equivalent $\sigma_{CF} \rightarrow \sigma_{CF}^*$ interactions. The $\sigma_{CC} \rightarrow \sigma_{CF}^*$ interactions are somewhat more strongly stabilizing (by 553 cm^{-1} each) than the $\sigma_{CF} \rightarrow \sigma_{CF}^*$ interactions (by 199 cm^{-1} each). In the puckered C_4F_8 geometry, the $\sigma_{CC} \rightarrow \sigma_{CF}^*$ interactions split into two sets, a set of eight stronger interactions involving the "equatorial" C−F_{β} antibonds ($\sigma_{CC} \rightarrow \sigma_{\beta}^*$) and a set of eight weaker interactions involving the "axial" C−F_{α} antibonds ($\sigma_{CC} \rightarrow \sigma_{\alpha}^*$). The $\sigma_{CF} \rightarrow \sigma_{CF}^*$ interactions similarly split into two sets, stronger $\sigma_{\alpha} \rightarrow \sigma_{\alpha}^*$ interactions and weaker $\sigma_{\beta} \rightarrow \sigma_{\beta}^*$.

The strongest of the key interactions in puckered C_4F_8 is between C−C bonds and equatorial C−F_{β} antibonds (at 1028 cm^{-1} each). Figure 9 shows a stereoview of one of these interactions. The bond orbital for the upper left C−C bond is shown as a light blue (positive amplitude) lobe that is slightly distorted (bent) to the outside of the strained four-member ring. The vicinal C−F_{β} antibond arises from the out-of-phase combination of C and F hybrid orbitals of roughly sp^3 and sp^2 character, respectively. Importantly, the backside of the C hybrid, also shown in blue, extends into the center of the ring, significantly penetrating the C−C bond orbital. The resulting overlap promotes $\sigma_{CC} \rightarrow \sigma_{\beta}^*$ delocalization and stabilizes the puckered form by 1028 cm^{-1}. The $\sigma_{CC} \rightarrow \sigma_{\alpha}^*$ interactions are weaker (213 cm^{-1}) because the axial orientation of the antibond directs the backside lobe of the C hybrid away from the center of the four-member ring, thereby decreasing bond−antibond overlap.

Figure 10 shows a stereoview of an "axial−axial" $\sigma_{\alpha} \rightarrow \sigma_{\alpha}^*$ interaction in puckered C_4F_8. One sees in the upper left-hand portion of this figure that the C−F_{α} bond is composed of two lobes, the major (blue) lobe in the bonding region and a minor (yellow) backside lobe of the F hybrid. No backside lobe appears for the C hybrid because this orbital is strongly polarized (73%) toward the more electronegative F atom so that amplitude at the C atom is weak. On the right is a C−F_{α} antibond. The orbital is strongly polarized toward the C atom and thereby reveals a

fairly large backside lobe at the C atom (in blue) that overlaps with the major lobe of the vicinal C−F_α bond. However, the resulting interaction (304 cm^{-1}) remains rather weak because the strong polarization of the C−F_α bond orbital toward F reduces the degree of overlap between these orbitals. The orbital overlap is even smaller in the "equatorial−equatorial" $\sigma_\beta \rightarrow \sigma_\beta^*$ interactions, which each stabilize puckered C_4F_8 by only 119 cm^{-1}.

The $\sigma_{CC} \rightarrow \sigma_{CF}^*$ and $\sigma_{CF} \rightarrow \sigma_{CF}^*$ interactions collectively stabilize puckered C_4F_8 by 13312 cm^{-1} and planar C_4F_8 by 12032 cm^{-1}. Thus, these hyperconjugative interactions are 1280 cm^{-1} more strongly stabilizing in the puckered than in the planar form. Clearly, in the absence of these interactions, C_4F_8 would instead favor a planar equilibrium geometry. Moreover, the extra stability of the puckered geometry arises predominantly as a result of the $\sigma_{CC} \rightarrow \sigma_{CF}^*$ interactions, which account for 1080 of the 1280 cm^{-1} stabilization.

Hyperconjugation also accounts for the smaller puckering barrier of C_4F_8 relative to that of C_4H_8. Whereas the $\sigma_{CC} \rightarrow \sigma_{CF}^*$ and $\sigma_{CF} \rightarrow \sigma_{CF}^*$ interactions provide 1280 cm^{-1} of extra stabilization for puckered C_4F_8, the $\sigma_{CC} \rightarrow \sigma_{CH}^*$ and $\sigma_{CH} \rightarrow \sigma_{CH}^*$ interactions of C_4H_8 (cf. Table 10) stabilize its puckered geometry by 3208 cm^{-1} relative to the planar form. The hyperconjugative interactions in C_4F_8 suggest a weaker geometry dependence than the corresponding interactions in C_4H_8 and are therefore responsible for the smaller inversion barrier in C_4F_8.

IV. Conclusions

Using a high-resolution FT spectrometer and supersonic expansion of perfluorocyclobutane in helium, we were able, for the first time, to record a rotationally resolved spectrum of *c*-C_4F_8. The rovibrational structures in two bands, ν_{12} and ν_{13}, were assigned and fit using a simple rigid rotor model. While the ν_{12} parallel band could be fit with a band origin and upper and lower state *B* rotational constants, the rovibrational transitions in the ν_{13} parallel band were all observed to be split by about 0.0018 cm^{-1}, suggesting a different set of ring-puckering selection rules for this band as compared to the ν_{12} band. In fact, the ν_{12} mode has b_2 symmetry under D_{2d} that correlates to a_{2u} symmetry under D_{4h} and consequently has $\pm \leftarrow \pm$ ring-puckering selection rules. Transitions from the ground state and occupied excited torsional states should overlap at the spectral resolution used here. The ν_{13} mode is b_2 symmetry under D_{2d} that correlates to b_{2g} under D_{4h}, and in this case, the ring-puckering selection rules are $\pm \leftarrow \mp$. Rotational transitions from the ground and first excited torsional states will be separated by the torsional splitting in the ground and excited vibrational states, and indeed, this is what we observe for the ν_{13} band. These results confirm the previous assignment by Miller and Capwell.

The structure, vibrational frequencies, and puckering barrier of C_4F_8 were evaluated at the MP2 and CCSD(T) levels of theory. Vibrationally averaged structural parameters calculated at the MP2/cc-pVQZ level compare favorably (within the experimental error bars) with values determined from previous electron diffraction studies, except for the puckering (dihedral) (C−C−C−C) angle of 14.6° that is somewhat smaller than the experimental value of 17.4°. Furthermore, the rotational constants estimated by applying the MP2/cc-pVDZ vibrational corrections to the MP2/cc-pVQZ optimal geometries are within 0.00002 cm^{-1} from the values determined experimentally in this study.

The anharmonic vibrational frequencies estimated at the MP2/cc-pVDZ level of theory using higher energy derivatives are in very good agreement with the experimentally observed fundamentals. The largest difference $|\nu_{calcd} - \nu_{exp}|$ is 27 cm^{-1} for the ν_1 mode, <15 cm^{-1} for the other ones, and in some cases <5 cm^{-1}. The exception is ν_2, the CF_2 antisymmetric stretching/rocking vibration, for which the difference is 127 cm^{-1}. This value is well outside the range for all others, a fact that may suggest a potential problem with the previous experimental assignment.

As in the case for C_4H_8, we observe a constant difference between the MP2 and the CCSD(T) magnitude of the ring-puckering barrier for the same basis set. We have relied on this observation to estimate CBS values at the CCSD(T) level of theory by adding this constant difference to the MP2 value for each basis set larger than cc-pVQZ for which CCSD(T) calculations are not currently feasible. The estimated MP2/CBS limit for the barrier is 189 cm^{-1}. Our best estimate for the ring-puckering barrier at the CCSD(T)/CBS level of theory is 132 cm^{-1}, considerably smaller than the corresponding barrier of 498 cm^{-1} that we previously reported for C_4H_8. NBO analysis reveals that the torsional strain typically associated with the puckering of four-member ring geometries stems, in fact, from differential stabilization of the puckered and planar geometries by hyperconjugation. Puckered C_4F_8 is stabilized by $\sigma_{CC} \rightarrow \sigma_{CF}^*$ hyperconjugative interactions as the backside lobes of the equatorial C−F_β antibonds penetrate vicinal C−C bonding orbitals. These interactions are less stabilizing in the planar form due to diminished orbital overlap. Our analysis further suggests that the smaller barrier height in C_4F_8 as compared to that of C_4H_8 results from weaker orbital interactions. Whereas axial−axial $\sigma_{CH} \rightarrow \sigma_{CH}^*$ interactions stabilize puckered C_4H_8 fairly strongly, the corresponding $\sigma_{CF} \rightarrow \sigma_{CF}^*$ interactions of puckered C_4F_8 are comparatively weak due to the strong polarization of the C−F_α orbital toward the more electronegative F atom and, hence, poor overlap with the vicinal C−F_α antibond.

Acknowledgment. Part of this work was performed in the William R. Wiley Environmental Molecular Sciences Laboratory (EMSL) under the auspices of the Division of Chemical Sciences, Office of Basic Energy Sciences, U.S. Department of Energy under Contract DE-AC06-76RLO 1830 with Battelle Memorial Institute, which operates the Pacific Northwest National Laboratory. The EMSL is a national user facility funded by the Office of Biological and Environmental Research in the U.S. Department of Energy. Computer resources were provided by the Division of Chemical Sciences, U.S. Department of Energy. E.D.G. acknowledges the Indiana State University Office of Information Technology for the use of their computer resources.

References and Notes

(1) Blackwell, C. S.; Lord, R. C. *Vib. Spectra Struct.* **1972**, *1*, 1.
(2) Lafferty, W. J. *Crit. Eval. Chem. Phys. Struct. Inf. Proc. Conf.*; National Academy of Sciences: Washington, DC, 1974; pp 386−409.
(3) Laane, J. *Q. Rev.* **1971**, *20*, 533.
(4) Laane, J. *Appl. Spectrosc.* **1970**, *24*, 73.
(5) Stone, J. M. R.; Mills, I. M. *Mol. Phys.* **1970**, *18*, 631.
(6) Ueda, T.; Simanuchi, T. *J. Chem. Phys.* **1968**, *49*, 470.
(7) Malloy, T. B., Jr.; Lafferty, W. J. *J. Mol. Spectrosc.* **1975**, *54*, 20.
(8) (a) Miller, F. A.; Capwell, R. J. *Spectrochim. Acta* **1971**, *27A*, 947. (b) Miller, F. A.; Capwell, R. J. *Spectrochim. Acta* **1972**, *28A*, 603.
(9) (a) Egawa, T.; Fukuyama, T.; Yamamoto, S.; Takabayashi, F.; Kambara, H.; Ueda, T.; Kuchitsu, K. *J. Chem. Phys.* **1987**, *86*, 6018. (b) Egawa, T.; Yamamoto, S.; Ueda, T.; Kuchitsu, K. *J. Mol. Spectrosc.* **1987**, *126*, 231. (c) Egawa, T.; Yamamoto, S.; Kuchitsu, K. *J. Mol. Spectrosc.* **1988**, *129*, 72.
(10) Li, H.; Miller, C.; Phillips, L. A.. *J. Chem. Phys.* **1994**, *100*, 8590.
(11) Blake, T. A.; Xantheas, S. S. *J. Phys. Chem. A* **2006**, *110*, 10487.

(12) Glendening, E. D.; Halpern, A. M. *J. Phys. Chem. A* **2005**, *109*, 635.

(13) Weinhold, F.; Landis, C. R. *Valency and Bonding*; Cambridge University Press: New York, 2005.

(14) Glendening, E. D.; Badenhoop, J. K.; Reed, A. E.; Carpenter, J. E.; Bohmann, J. A.; Morales, C. M.; Weinhold, F. *NBO 5.G*; Theoretical Chemistry Institute, University of Wisconsin: Madison, WI, 2001; http://www.chem.wisc.edu/~nbo5.

(15) (a) Claassen, H. H. *J. Chem. Phys.* **1950**, *18*, 543. (b) Miller, F. A.; Capwell, R. J. *Spectrochim. Acta* **1971**, *27A*, 1113. (c) Miller, F. A.; Wolanin, J. A. *Spectrochim. Acta* **1975**, *31A*, 1427. (d) Harris, W. C.; Coe, D. A.; Pringle, W. C., Jr.; Snow, J. K. *J. Mol. Spectrosc.* **1976**, *62*, 149.

(16) Chang, C. H.; Porter, R. F.; Bauer, S. H. *J. Mol. Struct.* **1971**, *7*, 89.

(17) Harris, W. C.; Yang, D. B. *J. Chem. Phys.* **1974**, *60*, 4175.

(18) Mao, C.; Niew, C.-S.; Zhu, Z.-Y. *Spectrochim. Acta* **1988**, *44A*, 1093.

(19) Fischer, G.; Purchase, R. L.; Smith, D. M. *J. Mol. Struct.* **1997**, *405*, 159.

(20) Dunning, T. H., Jr. *J. Phys. Chem.* **2000**, *104*, 9062 and references therein.

(21) (a) Dunning, T. H., Jr. *J. Chem. Phys*. **1989**, *90*, 1007. (b) Kendall, R. A.; Dunning, T. H., Jr.; Harrison, R. J. *J. Chem. Phys*. **1992**, *96*, 6796.

(22) (a) Clabo, D. A., Jr.; Allen, W. D.; Remington, R. B.; Yamaguchi, Y.; Schaefer, H. F., III. *Chem. Phys*. **1988**, *123*, 187−239. (b) Allen, W. D.; Yamaguchi, Y.; Császár, A. G.; Clabo, D. A., Jr.; Remington, R. B.; Schaefer, H. F., III. *Chem. Phys*. **1990**, *145*, 427−466. (c) Miller, W. H.; Hernandez, R.; Handy, N. C.; Jayatilaka, D.; Willets, A. *Chem. Phys. Lett*. **1990**, *172*, 62−68. (d) Barone, V. *J. Chem. Phys*. **2004**, *120*, 3059−3065. (e) Barone, V. *J. Chem. Phys*. **2005**, *122*, 014108.

(23) (a) Barone, V. *J. Chem. Phys*. **1994**, *101*, 10666−10676. (b) Minichino, C.; Barone, V. *J. Chem. Phys*. **1994**, *100*, 3717−3741. (c) Barone, V.; Minichino, C. *THEOCHEM* **1995**, *330*, 365−376.

(24) Frisch, M. J.; Trucks, G. W.; Schlegel, H. B.; Scuseria, G. E.; Robb, M. A.; Cheeseman, J. R.; Zakrzewski, V. G.; Montgomery, J. A., Jr.; Stratmann, R. E.; Burant, J. C.; Dapprich, S.; Millam, J. M.; Daniels, A. D.; Kudin, K. N.; Strain, M. C.; Farkas, O.; Tomasi, J.; Barone, V.; Cossi, M.; Cammi, R.; Mennucci, B.; Pomelli, C.; Adamo, C.; Clifford, S.; Ochterski, J.; Petersson, G. A.; Ayala, P. Y.; Cui, Q.; Morokuma, K.; Malick, D. K.; Rabuck, A. D.; Raghavachari, K.; Foresman, J. B.; Cioslowski, J.; Ortiz, J. V.; Stefanov, B. B.; Liu, G.; Liashenko, A.; Piskorz, P.; Komaromi, I.; Gomperts, R.; Martin, R. L.; Fox, D. J.; Keith, T.; Al-Laham, M. A.; Peng, C. Y.; Nanayakkara, A.; Gonzalez, C.; Challacombe, M.; Gill, P. M. W.; Johnson, B. G.; Chen, W.; Wong, M. W.; Andres, J. L.; Head-Gordon, M.; Replogle, E. S.; Pople, J. A. *Gaussian 98*, revision A.9; Gaussian, Inc.: Pittsburgh, PA, 1998.

(25) MOLPRO is a package of ab initio programs written by H.-J. Werner and P. J. Knowles, with contributions from R. D. Amos, A. Bernhardsson, A. Berning, P. Celani, D. L. Cooper, M. J. O. Deegan, A. J. Dobbyn, F. Eckert, C. Hampel, G. Hetzer, T. Korona, R. Lindh, A. W. Lloyd, S. J. McNicholas, F. R. Manby, W. Meyer, M. E. Mura, A. Nicklass, P. Palmieri, R. Pitzer, G. Rauhut, M. Schütz, H. Stoll, A. J. Stone, R. Tarroni, and T. Thorsteinsson.

(26) Anchell, J.; et al. *NWChem, A Computational Chemistry Package for Parallel Computers*, Version 4.0; Pacific Northwest National Laboratory: Richland, Washington, 1999.

(27) (a) Feller, D. *J. Chem. Phys.* **1992**, *96*, 6104. (b) Xantheas, S. S.; Dunning, T. H., Jr. *J. Phys. Chem.* **1993**, *97*, 18. (c) Xantheas, S. S.; Dunning, T. H., Jr. *J. Phys. Chem.* **1993**, *97*, 6616.